Research Square

Preprints are preliminary reports that have not undergone peer review.
They should not be considered conclusive, used to inform clinical practice,
or referenced by the media as validated information.

Role of surface roughness in load transfer of rock-socketed piles: a 3D-Printed interface investigation

[redacted]

cryaqvtc@163.com

Anqing Vocational and Technical College

Yueping Chen

Anqing Vocational and Technical College

Fei Jin

Anqing Vocational and Technical College

Weimin Wang

Hefei University of Technology

Min He

Hefei University of Technology

Yonggao Yin

Hefei University of Technology

Research Article

Keywords: Deep rock-socketed piles, PRI roughness, Bearing mechanism, Model tests

Posted Date: March 12th, 2026

DOI: https://doi.org/10.21203/rs.3.rs-9040310/v1

License: This work is licensed under a Creative Commons Attribution 4.0 International License.
Read Full License

Additional Declarations: No competing interests reported.

Role of surface roughness in load transfer of rock-socketed piles: a 3D-Printed interface investigation

Abstract： Deep rock-socketed piles (DRSPs) play a vital role in deep foundation engineering, where the pile-rock interface (PRI) behavior critically governs the bearing performance and safety of the pile. To address the limited understanding of the load-transfer mechanism in DRSPs, five sets of laboratory model tests were conducted to simulate the bearing behavior under varying PRI roughness factor (RF). The tests revealed a consistent failure mechanism across different RF conditions: radial cracks formed on the bedrock surface, asperities at the PRI were sheared off, and punching failure occurred at the pile top. With increasing RF, the number of cracks and the volume of sheared rock increased, while the depth of shear failure at the pile tip decreased. The base angle of the triangular failure zone progressively shifted from 45° toward 90° . Displacement measurements indicated that pile tip settlement was inversely related to RF. A higher RF was associated with a greater ultimate bearing capacity of the pile. In addition, the attenuation rate of axial force along the pile shaft increased with RF. Shaft resistance was mobilized earlier in the shallow section compared to the deeper section. As RF increased, the ultimate shaft resistance provided by the PRI also rose, thereby improving the overall bearing capacity of the DRSPs. The findings from this experimental study offer valuable insights for the design and construction of DRSPs.

Keywords: Deep rock-socketed piles, PRI roughness, Bearing mechanism, Model tests

Highlights

1.Revealed roughness-dependent failure mechanisms in deeply rock-socketed piles (DRSPs), showing increased roughness leads to more radial cracks, greater asperity shearing, and reduced tip failure depth.

2.Established a positive correlation between roughness factor (RF) and ultimate bearing capacity, with a 0.1 increase in RF boosting capacity by 20% and reducing settlement by 18%.

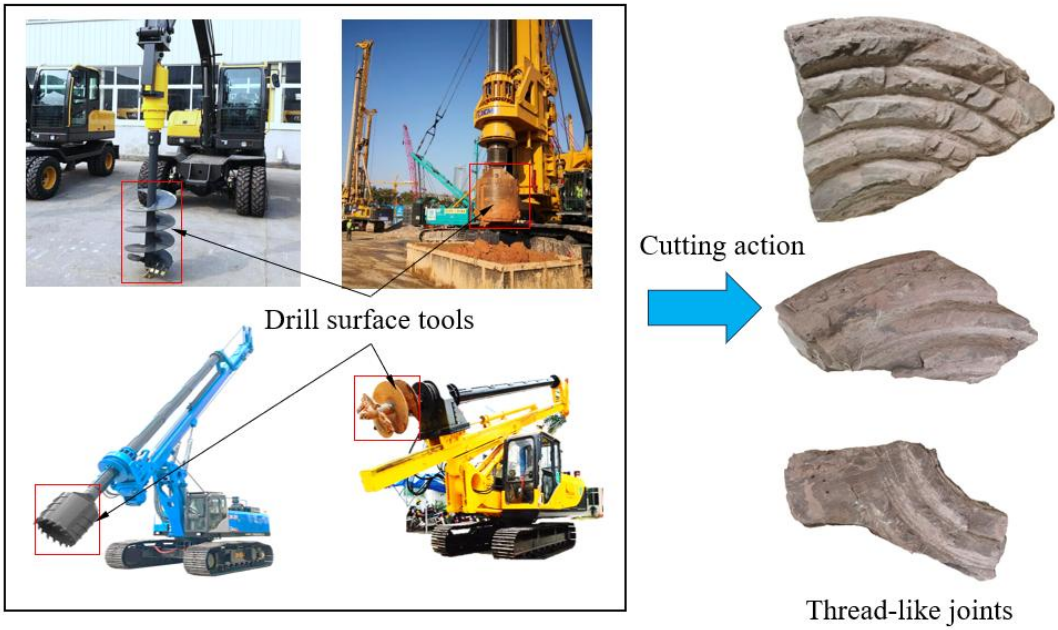
3.Developed a predictive model for DRSP capacity incorporating RF, pile diameter,

elastic modulus, socket depth, and rock strength, validated with experimental and field data.

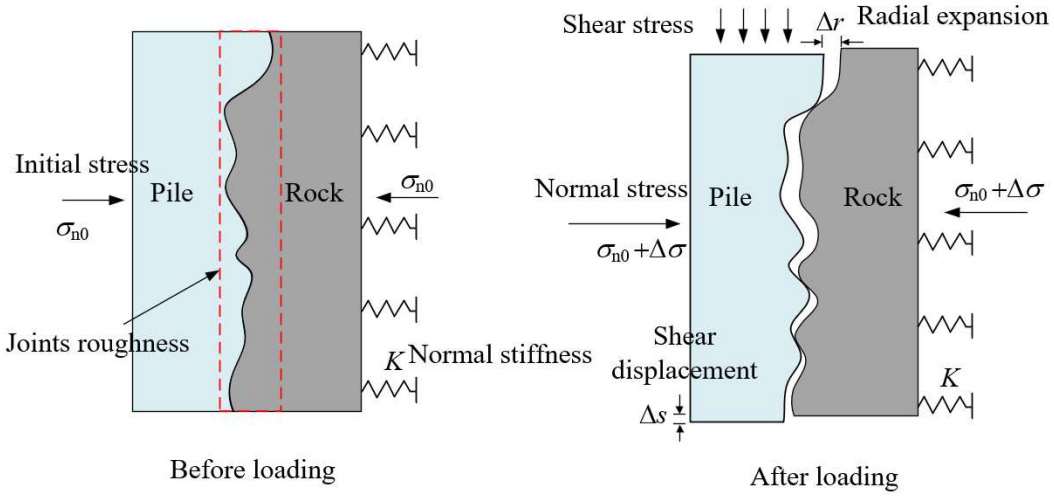
1 Introduction

Rock-socketed piles (RSPs) constitute a specialised foundation system distinguished by their high load-bearing capacity, limited settlement, and efficient load-transfer mechanism, thereby meeting the rigorous performance demands imposed by bridge structures (Wang et al. 2023; Akguner and Kirkit 2011; Xing et al. 2014). The escalating loads from superstructures pose a significant challenge, as conventional RSPs often prove inadequate to fulfil the stringent demands for high bearing capacity and limited deformation under the extreme conditions of long-span rail-cum-road bridges (Rui et al. 2011; Kulkarni and Dewaikar 2019; Li et al. 2021; Sun et al. 2024; Xu et al. 2022). Consequently, deeply rock-socketed piles (DRSPs), characterised by a socket length-to-diameter ratio (h_r/D) of 5 or greater, are seeing growing adoption in major projects. Nonetheless, their intrinsic construction method introduces distinct challenges. Specifically, the rotary action of the drilling rig's teeth during the boring process inevitably generates a series of irregular protrusions on the borehole wall, as depicted in Fig. 1(a). This inherent roughness results in a distinct pile-rock interface (PRI) with the cast-in-place concrete shaft, which is markedly different from a smooth plane, as shown in Fig. 1(b). Compared to the idealised smooth interfaces typically assumed in design codes, the presence of PRI roughness significantly alters the distribution of frictional resistance and the interfacial shear behaviour (Murali et al. 2024; Sivaraman and Kumaran 2023; Xing et al. 2017; Zhang and Xue 2024). The load-sharing mechanism between the shaft and base is driven by interface roughness, which causes their asynchronous mobilisation and leads to behaviour distinct from standard design assumptions. Moreover, significant loading can induce sliding along the borehole wall's protrusions. The consequent large deformations prompt a radial expansion of the pile shaft, generating additional normal stress at the PRI–a phenomenon known as the 'dilatancy effect' that modifies the load-transfer mechanism and increases friction. The

failure of current design codes to account for this combined influence of roughness and dilatancy results in a substantial underestimation of the vertical bearing capacity of DRSPs.



(a) Rotary drilling rig



(b) PRI roughness

Fig. 1 Rotary drilling rig and PRI roughness

Regarding the mechanical characteristics of DRSPs, previous studies have primarily investigated their key influencing factors through numerical simulation, theoretical analysis, and numerical calculation methods. Singh et al. (2017) performed numerical analysis on the behavior of RSPs under independent and combined loads using PLAXIS3D, focusing on the effect of combined loads on the bearing capacity

behavior of RSPs. Ai and Chen (2020) analyzed the bearing characteristics of piles embedded in multi-layered rock by means of finite element-boundary element coupling analysis method, and the study showed that the top settlement is inversely proportional to the ratio of rock-socketed depth and directly proportional to the pile-rock mass ratio, modulus ratio and pile length-diameter ratio. Seol et al. (2009) coded the load transfer model of pile-soil and PRIs with user subroutine FRIC and imported them into ABAQUS, and the simulation results were highly consistent with the field observation results. To address the bearing capacity design of rRSPs, Liang et al. (2024) developed a micromechanical PRI model that integrates the slip line method with the Hoek-Brown criterion. This model was implemented numerically via a user-defined FRIC subroutine in ABAQUS and successfully applied to analyse RSPs embedded in soft rock strata. Through direct shear tests, Chen et al. (2025) investigated the influence of interface roughness and concrete setting stress on the shear strength of the PRI. They established a functional relationship between the interface strength parameters and the pile depth, which was subsequently incorporated into FLAC^{3D} to refine the bearing capacity model for RSPs. Gutiérrez-Ch et al. (2025) observed more detailed load distribution of RSPs by measuring PRI "slice" with discrete element tool. Zhao et al. (2024) incorporated an interfacial shear model that accounts for the random distribution pattern of rock fractures into the load-transfer equation for RSPs, and investigated the influence of the degree of rock fracturing on the distribution of side resistance and the settlement behaviour of RSPs. Xing et al.(2017) developed an analytical method for the radius of plastic zone around pile based on cavity expansion theory and shear strength theory, and the study showed that the axial force of pile shaft was affected by pile diameter, Poisson ratio of rock and rock properties. Zhao et al. (2017)and Zhao et al.(2014) considered the influence of roughness on PRI behavior, and the study showed that interface roughness is the main factor affecting lateral resistance, and increasing the normal stiffness of hole wall is beneficial to mobilize lateral resistance. Hou et al. (2022) also believed that roughness and rock characteristics have significant influence on PRI shear behavior through upper and lower limit analysis. Liu et al. (2023) introduced

roughness factor (RF) to describe hole wall roughness based on measured hole wall section characteristics, and proposed an analytical solution of side resistance of r RSPs considering hole wall roughness. The reliability of theoretical model was verified by field measured data. The above studies focus on numerical simulation and theoretical studies. However, model tests are also considered as reliable means to study the bearing mechanism of RSPs. Dai et al. (2017) designed 5 piles with different roughness, and found that the ultimate unit side resistance of pile shaft increases greatly with the increase of side wall roughness and rock stiffness. Gutiérrez-Ch et al. (2021) designed centrifuge test of RSPs, and the study showed that the greater the roughness, the more loads would be initially attracted to the upper part of piles, and these loads would tend to move downward with the continuous increase of pile head load. Wang et al. (2011) carried out model test of bearing mechanism of RSPs in red sandstone, and found that the frictional resistance of RSPs in red sandstone was distributed in inverted triangle shape. Liu et al. (2025) showed through field load testing that the larger the RF, the greater the moving shaft resistance.

The aforementioned studies are based on idealised roughness models; however, they do not account for the three-dimensional nature of actual roughness encountered in engineering practice (Sun et al. 2024; Yan et al. 2025; Zhang et al. 2025; Zhao et al. 2024). The load-bearing behaviour of DRSPs is critical to the stability of long-span bridges. Understanding the relationship between the load-transfer mechanism and interface roughness forms the core of this study, which investigates DRSPs within the engineering context of the Chizhou Changjiang River Rail-highway Bridge. A series of model tests on five DRSPs with different RF were conducted to examine the relationship between interface roughness and bearing capacity. The deformation and mechanical characteristics of the piles were analysed, with the aim of summarising the influence of roughness on the load-transfer mechanism. The findings are expected not only to guide the design and construction of DRSPs for long-span bridges but also to enrich the existing theory of pile foundations.

2 Model test design of DRSPs

The Chizhou Yangtze River Highway-Rail Bridge connects Zongyang County of Tongling City and Guichi District of Chizhou, which is a comprehensive traffic project spanning the Yangtze River, as shown in Fig. 2. The total length of the Chizhou Yangtze River Highway-Rail Bridge is 3,108.5 meters. The main bridge is a double-deck steel truss cable-stayed structure carrying both highway and railway traffic, with a span arrangement of (100 + 378 + 812 + 364 + 114) m. The approach bridges on the north bank feature simply-supported steel truss composite beams with a span of 140 m, while other approach spans utilize concrete beams with spans of 40.7 m and 32.7 m, respectively. According to Section 4 of Anhui Chizhou Yangtze River Highway-Rail Bridge CZDQ-1 Pile Test Project Test Report, a group of test piles shall be respectively conducted at 40.7m span of north bank approach bridge and 32.7m span of south bank approach bridge. If the range difference of two test piles exceeds the average value by 30% or the low value is less than the theoretical calculation value, standby test piles shall be added. Non-in-situ piles shall be adopted for test piles, mainly to verify the rationality of design parameters of each soil layer and the ultimate bearing capacity of single pile. The diameter of the test pile is 1.25 m, the concrete strength grade is C30, the design pile length is 60 m, and the rock-socketed depth is about 15 m.

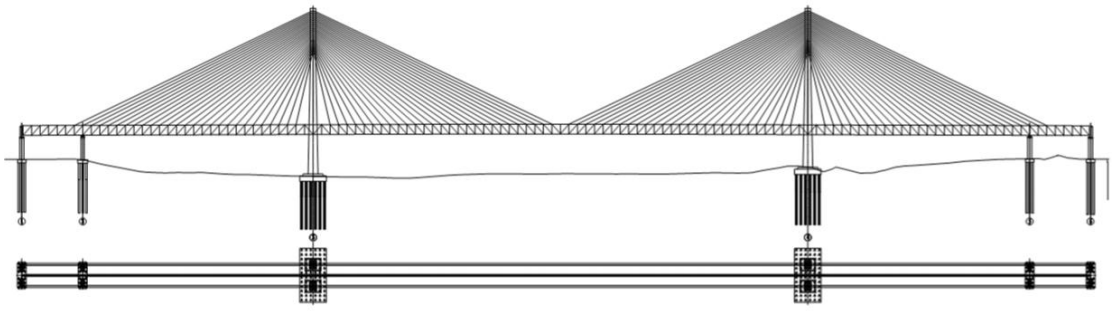


Fig. 2 Chizhou Yangtze River Highway-Rail Bridge

2.1 Similarity ratio design

There is a certain proportion between model test and full size test (Huang et al. 2019; Huang et al. 2021). The similarity ratio of model box is designed to satisfy the boundary condition of simulating model pile. According to the second similarity theorem (i.e. π

148 theorem), by selecting length L, density ρ and stress σ as independent fundamental
149 dimensional parameters, the similarity ratio constants C_{L}, C_{ρ} and C_{σ} can uniquely
150 determine the similarity relationship of other physical quantities. These three
151 independent fundamental physical quantities can constitute dimensionless p numbers
152 of other physical quantities (Yalin 1971; Takahashi and Ikeno 2024)

$$f\left(L,u,A,\rho,\sigma,\varepsilon,E,v,\varphi,C,F,P\right)=0 \tag{1}$$

153 where L is length, u is displacement, A is sectional area, ρ, σ, φ, C are density, stress,
154 internal friction angle, cohesion, v, ε are Poisson's ratio and strain, F and P are
155 concentrated load and surface load, respectively. By introducing the equilibrium
156 differential equation of elastic mechanics, the constraint conditions among the three can
157 be established (Goodier and Thomson 1944)

$$\begin{cases} \dfrac{\partial\left(\sigma_x\right)_{\mathrm{p}}}{\partial x_{\mathrm{p}}}+\dfrac{\partial\left(\tau_{yx}\right)_{\mathrm{p}}}{\partial y_{\mathrm{p}}}+\dfrac{\partial\left(\tau_{zx}\right)_{\mathrm{p}}}{\partial z_{\mathrm{m}}}+\left(f_x\right)_{\mathrm{p}}=0 \\ \dfrac{\partial\left(\tau_{xy}\right)_{\mathrm{p}}}{\partial x_{\mathrm{p}}}+\dfrac{\partial\left(\sigma_y\right)_{\mathrm{p}}}{\partial y_{\mathrm{p}}}+\dfrac{\partial\left(\tau_{zy}\right)_{\mathrm{p}}}{\partial z_{\mathrm{p}}}+\left(f_y\right)_{\mathrm{p}}=0 \\ \dfrac{\partial\left(\sigma_{xz}\right)_{\mathrm{p}}}{\partial x_{\mathrm{p}}}+\dfrac{\partial\left(\tau_{yz}\right)_{\mathrm{p}}}{\partial y_{\mathrm{p}}}+\dfrac{\partial\left(\sigma_z\right)_{\mathrm{p}}}{\partial z_{\mathrm{p}}}+\left(f_z\right)_{\mathrm{p}}=0 \end{cases} \tag{2}$$

$$\begin{cases} \dfrac{\partial\left(\sigma_x\right)_{\mathrm{m}}}{\partial x_{\mathrm{m}}}+\dfrac{\partial\left(\tau_{yx}\right)_{\mathrm{m}}}{\partial y_{\mathrm{m}}}+\dfrac{\partial\left(\tau_{zx}\right)_{\mathrm{m}}}{\partial z_{\mathrm{m}}}+\left(f_x\right)_{\mathrm{m}}=0 \\ \dfrac{\partial\left(\tau_{xy}\right)_{\mathrm{m}}}{\partial x_{\mathrm{m}}}+\dfrac{\partial\left(\sigma_y\right)_{\mathrm{m}}}{\partial y_{\mathrm{m}}}+\dfrac{\partial\left(\tau_{zy}\right)_{\mathrm{m}}}{\partial z_{\mathrm{m}}}+\left(f_y\right)_{\mathrm{m}}=0 \\ \dfrac{\partial\left(\sigma_{xz}\right)_{\mathrm{m}}}{\partial x_{\mathrm{m}}}+\dfrac{\partial\left(\tau_{yz}\right)_{\mathrm{m}}}{\partial y_{\mathrm{m}}}+\dfrac{\partial\left(\sigma_z\right)_{\mathrm{m}}}{\partial z_{\mathrm{m}}}+\left(f_z\right)_{\mathrm{m}}=0 \end{cases} \tag{3}$$

158 The similarity relations between the similarity ratio constants C_{L}, C_{ρ}, C_{σ} and other
159 physical quantities can be expressed as:

$$\begin{aligned} &\text{Geometric similarity ratio: } C_{\mathrm{L}}=\frac{L_{\mathrm{p}}}{L_{\mathrm{m}}}=\frac{x_{\mathrm{p}}}{x_{\mathrm{m}}}=\frac{y_{\mathrm{p}}}{y_{\mathrm{m}}}=\frac{z_{\mathrm{p}}}{z_{\mathrm{m}}} \\ &\text{Density similarity ratio: } C_{\rho}=\frac{f_{\mathrm{p}}}{f_{\mathrm{m}}}=\frac{\left(f_x\right)_{\mathrm{p}}}{\left(f_x\right)_{\mathrm{m}}}=\frac{\left(f_y\right)_{\mathrm{p}}}{\left(f_y\right)_{\mathrm{m}}}=\frac{\left(f_z\right)_{\mathrm{p}}}{\left(f_z\right)_{\mathrm{m}}} \end{aligned} \tag{4}$$

$$\text{Stress similarity ratio: } C_\sigma = \frac{\sigma_p}{\sigma_m} = \frac{(\sigma_x)_p}{(\sigma_x)_m} = \frac{(\sigma_y)_p}{(\sigma_y)_m} = \frac{(\sigma_z)_p}{(\sigma_z)_m}$$

Conjunction (1) and (3) can be obtained

$$\frac{C_\sigma}{C_L C_\rho} = 1, C_\sigma = C_L C_\rho \tag{5}$$

Therefore, as long as any two of C_L, C_ρ and C_σ are determined, the third item can be determined. Combined with the actual conditions of the laboratory site and the feasibility of the test, the size similarity parameter of the test model box is designed as $C_L = 75$. Considering the limitations of the actual test equipment and test materials, the similarity ratio parameters of the model piles are determined as shown in

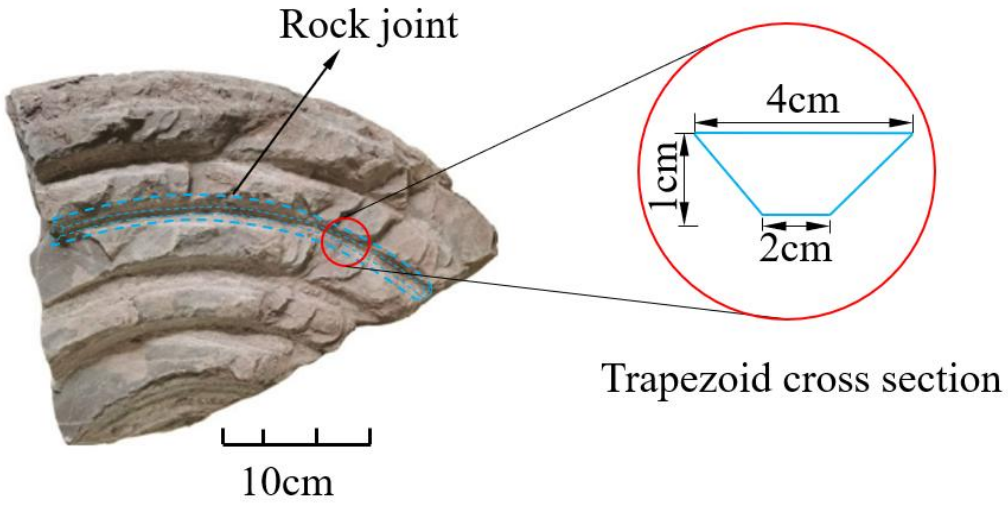
Table. **1**.

Table. 1 Scale relationships for model tests

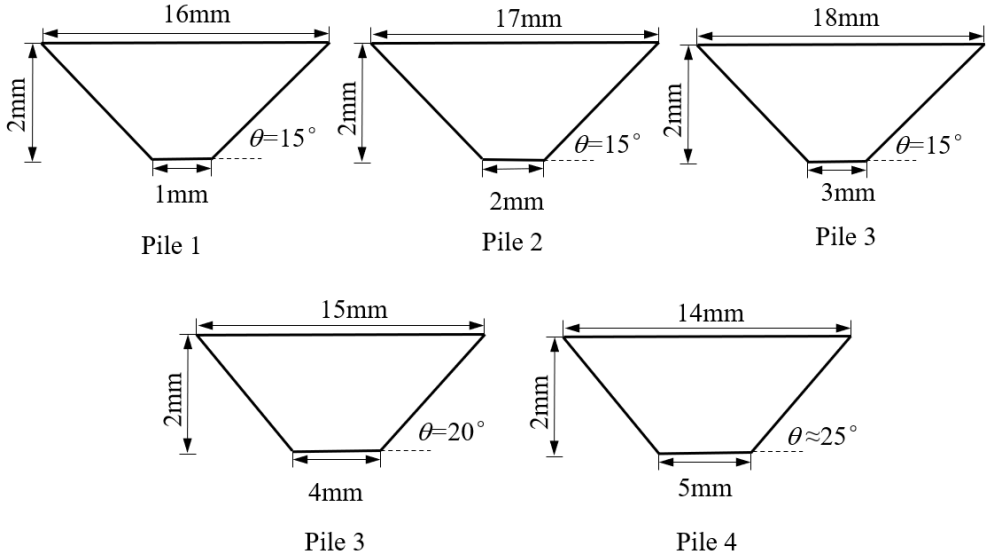
Type	Diameter /m	Prototype /m	Density / (kg/m^3)	Cohesive /kPa	Friction angle /(°)	Poisson's ratio	Elasticity modulus /GPa
Prototype	1.25	60	2500	2000	38.5	0.2	210
Model	0.02	0.25	1150	200	38.5	0.2	28.3

2.2 Roughness and model pile design

As shown in Fig. 3(a), no matter what kind of rotary drilling rig, the bit surface is equipped with cutting tools. Under the applied rotational torque, the cutting tools periodically engage with and cut the rock, thereby generating a series of regular asperities on the borehole wall. Examination under magnification reveals that an individual asperity possesses a cross-sectional geometry approximating an inverted trapezoid, as shown in Fig. 3(a).



(a) Asperities section



(b) Asperities section scale

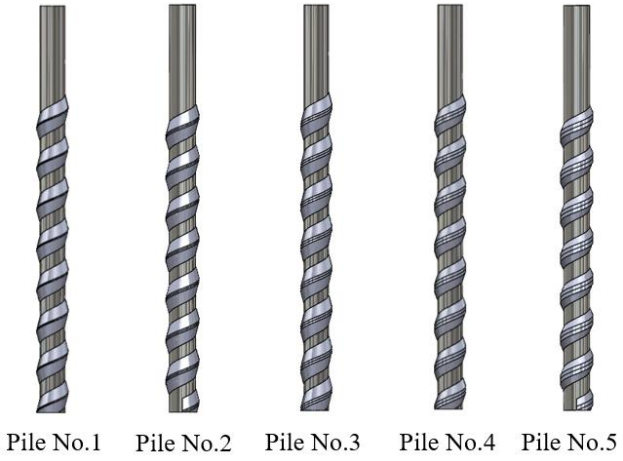
Fig. 3 Roughness design of five piles

A set of five model piles was designed to study the effect of PRI roughness on the bearing characteristics of DRSPs. The surface roughness of the models was designed to replicate the morphology of in-situ rock joints produced by rotary drilling, as shown in Fig. 3(b). The cross-section of rock joint roughness is inverted trapezoid. Horvath et al. (1980) defined a RF to describe the roughness of the rock-concrete interface of the rock socket:

$$\mathrm{RF} = \frac{h_{\mathrm{m}} L_{\mathrm{t}}}{RL} \tag{6}$$

where h_{m} is the average roughness height, L_{t} is the total stroke length along the sidewall profile, R is the nominal radius of the socket, and L is the nominal length of the socket.

In accordance with the similarity theory, the model pile had a length of 250 mm and a diameter of 20 mm. The threaded roughness was applied over a 200 mm length from the pile base, comprising 8 complete circles around the shaft. The top 50 mm of the pile surface remained smooth to facilitate the application of load. The 3D geometric model of the pile and roughness is drawn in SolidWorks in advance (Fig. 4(a)), and then the model pile with roughness is prepared by 3D printing, as shown in Fig. 4 (b) and (c).



(a) Model piles and roughness mapping



(b) Model pile 3D printing



(c) Model piles with different roughness

Fig. 4 Preparation process of model pile with roughness

The procedure commenced with exporting the digital model to an STL file. Critical printing parameters—layer height, infill density, printing temperature, and support structure settings—were then assigned using slicing software. Meticulous attention was paid to process control: the hotbed was levelled, first-layer adhesion was monitored in real-time, and a stable temperature was maintained within a closed build chamber. Post-printing, support structures were carefully removed, and the model pile surface was finished by sanding to remove all printing artefacts.

2.3 Materials

2.3.1 Piles

The material selected to model the pile foundation was a solid nylon rod (FS33000PA), chosen for its ability to simulate practical pile behaviour. Nylon possesses high strength, stiffness, good wear resistance, and sufficient flexibility to represent the deformation characteristics of an engineering pile. Furthermore, its good machinability allows the surface roughness to be accurately characterised according to experimental needs, enabling detailed observation of the pile-rock interaction. The material parameters of nylon rod (FS33000PA) are shown in Table. 2.

Table. 2 Material parameters of nylon rod (FS 33000PA)

Material parameter	Unit	Value
Density	g/cm^3	1.04
Compressive strength,	MPa	42
Tensile strength	MPa	46

Shear strength	MPa	19
Elasticity modulus	GPa	1.5
Bending strength	MPa	46.3
Flexural modulus	MPa	1300
Friction coefficient	-	0.2
Temperature range	℃	-40℃~80℃
Thermal expansion coefficient	-	8×10^{-5}/℃
Surface hardness	R	110~115

2.3.2 Overburden layer

Clean river sand was selected for the overburden layer owing to its common use as a geotechnical material and its advantages of uniform particle size, smooth surface, and moderate interparticle friction. The dried river sand was subjected to particle size distribution analysis. According to the Geotechnical Design Codes of Practice (Arnold et al. 2012), pass a certain mass of river sand through a series of screens with different apertures (0.1mm-10mm) for screening, and then calculate the weight percentage of each particle according to the mass of residual sand on each screen to obtain the particle grading curve. The particle grading curve of the river sand tested is shown in Fig. 5.

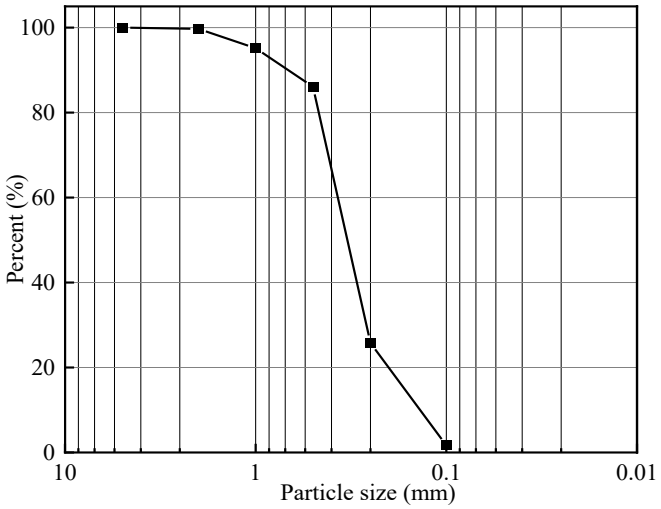


Fig. 5 Particle size distribution curve of river sand

The density of river sand is determined as follows: the nonuniformity coefficient C_u and curvature coefficient C_c of river sand are 2.6 and 1.2 respectively. The internal friction angle of river sand is 36.7° .The physical parameters of river sand are shown in Table. 3.

Table. 3 Physical parameters of river sand

Density/（g/cm^3）	Effective particle size/mm	Average particle size/mm	Restricted particle size/mm	Curvature coefficient	Coefficient of nonuniformity
1.57	0.15	0.35	0.39	1.2	2.6

2.3.3 Bedrock

The bearing stratum at the base of the test pile on the north bank is slightly to moderately weathered silty mudstone. Classified as a soft rock, it has a compressive strength of approximately 4MPa. The low strength of this bedrock was simulated in the test, drawing on established practices for selecting rock materials in the design of rock-socketed piles (Wan et al. 2024; Dykeman and Valsangkar 1996; Johnston and Choi 1986), they found that the properties of mixed materials composed of cement, river sand, water and accelerator are similar to those of weakly weathered silty mudstone at the bottom of bearing stratum of test pile. Finally, the mixture ratio of cement: sand: water: accelerator = 1:10: 2.275: 0.02 is selected, and the cement mortar is formed by uniform mixing. The cement is Conch brand Portland 425 cement, and the sand is clean river sand. The pouring process of deep embedded rock model is shown in Fig. 6.

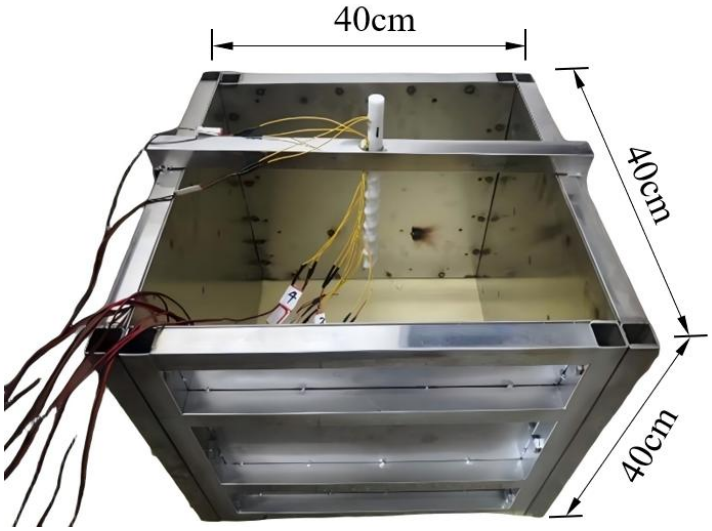


Fig. 6 Casting process of DRSPs model

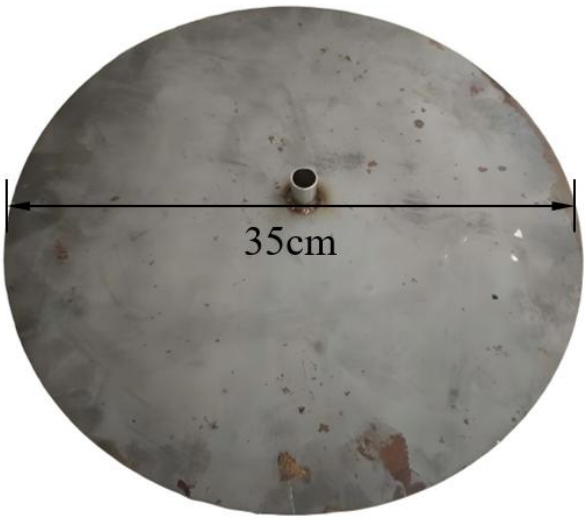
After curing for 7 days under standard conditions, the strength of bedrock is 1.2 MPa, elastic modulus is 0.35 GPa, Poisson ratio is 0.32. The cohesion of bedrock is 274 kPa and internal friction angle is 36.7°.

2.3.4 Model box and loading device

A custom-designed model box was employed for the experiments. The cubic container, with internal dimensions of 400 × 400 × 400 mm, was fabricated from 10-mm-thick Q235 steel plate using a continuous weld, as shown in Fig. 7 (a). To enhance the rigidity of the model box, eight square steel sections were installed on its four sides as strengthening supports, which were connected using high-strength bolts. The test pile was positioned at the geometric centre of the box. A rock block length of 20 cm (Rock-socketed ratio h_r=10) was used, and a 20 cm thick intact rock stratum was reserved at the pile end to simulate actual engineering conditions. Considering the influence of rock-soil boundary effect, according to Saint-Venant principle (Xu et al. 1997), stress disturbance can be ignored when the influence range of rock-soil around the pile exceeds 20 times of pile diameter. In this test, the pile diameter is set to 2 cm, and the unilateral length of model box is 40cm, which can ensure that the boundary in each direction is more than 20cm away from the pile center, so as to meet the boundary requirements.



(a) Model box



(b) Load plate



(c) load

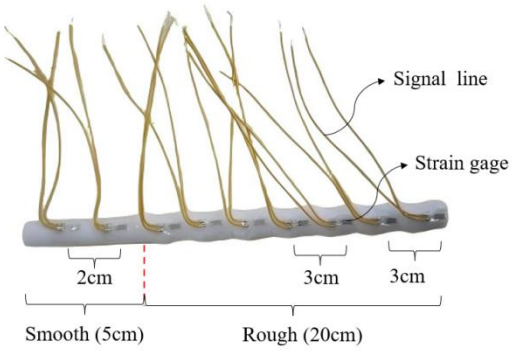
Fig. 7 Model box and loading system

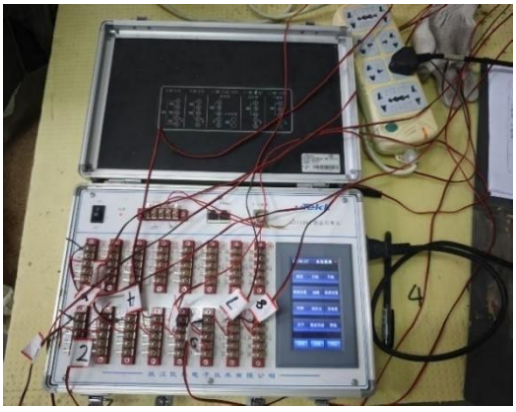
253 The model pile was loaded using a conventional setup. A purpose-built loading plate,
254 illustrated in Fig. 7(b), was employed. To accommodate the small diameter of the model
255 pile, a tray was installed on top to increase the loading area. A cylinder with a diameter
256 slightly larger than that of the pile was welded to the centre of the tray's underside. This
257 cylinder was inserted into the pile head during testing to restrain the tray's lateral
258 movement and ensure uniform load transfer. The load was applied using standard 100
259 ×100×300 mm prismatic test blocks, each weighing approximately 10 kg, as shown
260 in Fig. 7 (c). A graded loading procedure was adopted, with each load increment set at
261 10% of the estimated ultimate capacity. The displacement was required to stabilise at

each stage in accordance with standard specifications to ensure the acquired data accurately reflected the load-transfer mechanism and bearing characteristics of the drilled DRSPs.

2.5 Data collection system

The axial force of DRSPs is monitored by pasting strain gauges on the pile shaft, as shown in Fig. 8(a). Ten groups of strain measuring points are arranged at intervals of 25mm along the axis of the pile shaft. BX120-3AA welding-free strain gauges are used for the test. The grid size is 3.0×2.5mm and the base is 7.5×3.5mm. The strain gauges have good moisture resistance and corrosion resistance, and the strain gauges adopt fiber reinforced base, and the surface is covered with a protective layer of H62 yellow copper foil with a thickness of 0.03 mm, so the sealing performance is good. The sequence of pasting strain gauges is as follows: First, use 400 grit sandpaper to polish the pile surface and wipe off dust with wet towel. After the moisture completely evaporates, apply glue evenly at the specified displacement. Immediately after the glue application, stick the strain gauge sensitive grid base and terminal to the pile surface along the axial direction of the pile and gently press. After that, wrap 2 circles of transparent adhesive tape around the pile body at the pasting position of strain gauge, and wrap multiple circles of waterproof adhesive tape around the two sections of transparent adhesive tape to prevent water from penetrating into the strain gauge during mortar casting. Finally, connect the wires on the strain gauge terminals to the outside of the model box. The wire connections are also waterproof. The axial strain of pile body is collected using Wuhan Youtai uT7116Y type 16 channel static strain gauge, as shown in Fig. 8(b). The range of static strain gauge is 0~±30000με, and the strain resistance is 60–1000Ω. The strain acquisition adopts the quarter-bridge connection mode, and all the measured data are displayed on the LED screen at the same time during the test, and the acquisition frequency is 1Hz.





(a) Strain gauge arrangement (b) uT7116Y strain collector



(c) Initial elevation measurement (d) Displacement meter measurement

Fig. 8 Collection of pile top settlement and strain

The vertical displacement of the pile top was measured using displacement transducers with a range of 0–50 mm and a sensitivity of 0.01 mm. Prior to installation, the initial elevation of the pile top was recorded, as shown in Fig. 8(c). Each transducer was mounted using a three-point positioning method: the transducer rod was rigidly connected to an extension rod, the end of which was attached via a universal joint to a MAG-200 magnetic base. The base was then secured to a reference beam using its integrated NdFeB magnet. Due to limited clearance above the pile, a rigid extension plate was attached to the loading plate, and its settlement was measured as a proxy for the pile top settlement, as shown in Fig. 8 (d). To ensure data reliability, two transducers were positioned symmetrically on the extension plate at ±90°, and the average of their readings was taken as the final settlement value. During the test, after each level of load is applied, the settlement value is read after the dial indicator pointer is stable.

2.6 Test procedure

The model test procedure for Drilled Rock-Socketed Piles (DRSPs) comprised five main steps.

(1) Bedrock pouring

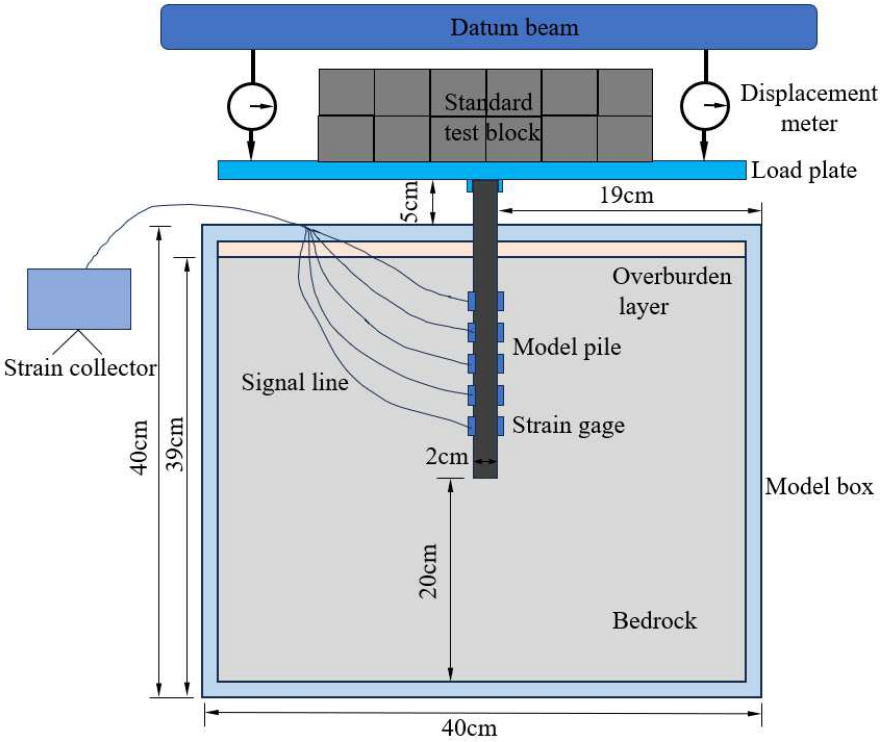
First, the inner walls of the model box were coated with engine oil. The bedrock material was then prepared as a cement mortar according to the specified mix ratio. This mixture was poured into the box in successive layers, with each layer's thickness controlled at 5 cm. Each layer was compacted for 30 seconds using a high-frequency vibrator. This process continued until a total bedrock height of 20 cm was achieved.

(2) Model pile embedding

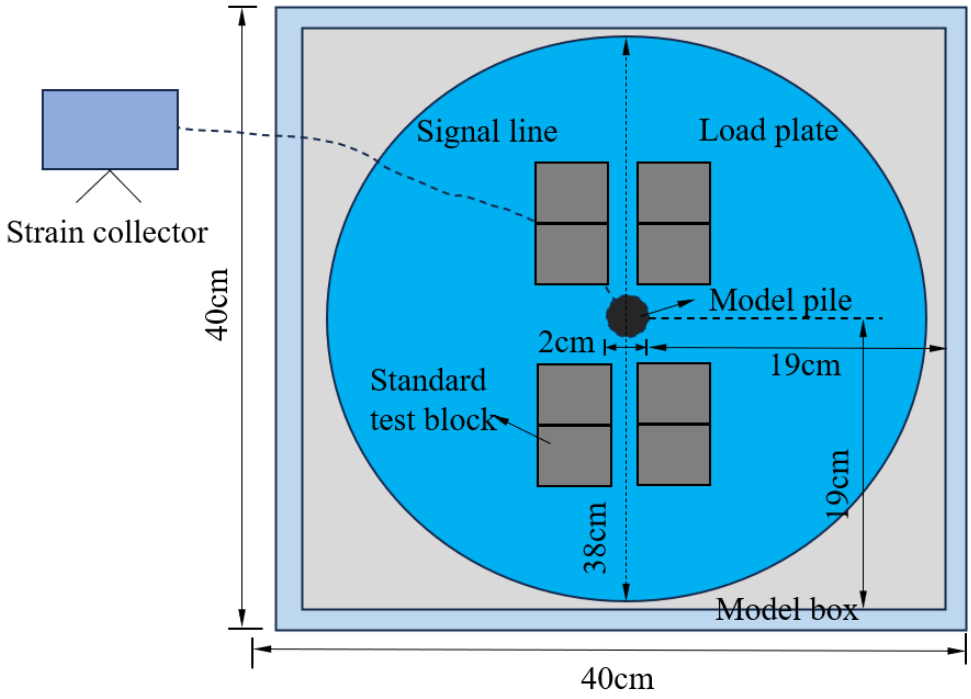
The model pile was fixed vertically at the centre of the box using metal clamps. To prevent segregation within the cement mortar, the rock stratum was poured in three successive layers, each with a height of 7 cm. Following the placement of each layer, the area around the pile was vibrated for 30 seconds using a hand-held vibrator. A 1 cm thick covering layer of river sand was placed near the top surface of the model box. Care was taken during vibration to avoid damaging the strain gauges and wiring. After pouring, the model was cured under standard conditions for 7 days.

(3) Measuring element installation

With the loading platform and extension plate assembled on the pile top, a DSB-50 dial gauge was installed on the reference beam and zeroed after contacting the plate. Strain gauges were connected via a quarter-bridge circuit, and initial readings were recorded following system balancing. The setup is detailed in the elevation and plan views of Fig. 9(a) and (b).



(a) Elevation



（b）Plan

Fig. 9 Elevation and plan of DRSPs model

(4) Gradation loading

Following the completion of the cement mortar curing, the DRSPs was subjected to a graded loading regime. At each stage, an equal number of counterweights were placed on the loading platform, and the load was maintained for 10 minutes until model pile failure occurred. The pile top settlement and strain gauge readings were recorded following the application of each load increment. Upon completion of the test, the counterweights were removed. The bedrock was then sectioned along its centreline to allow for observation of the PRI failure mode.

(5) Repeated tests

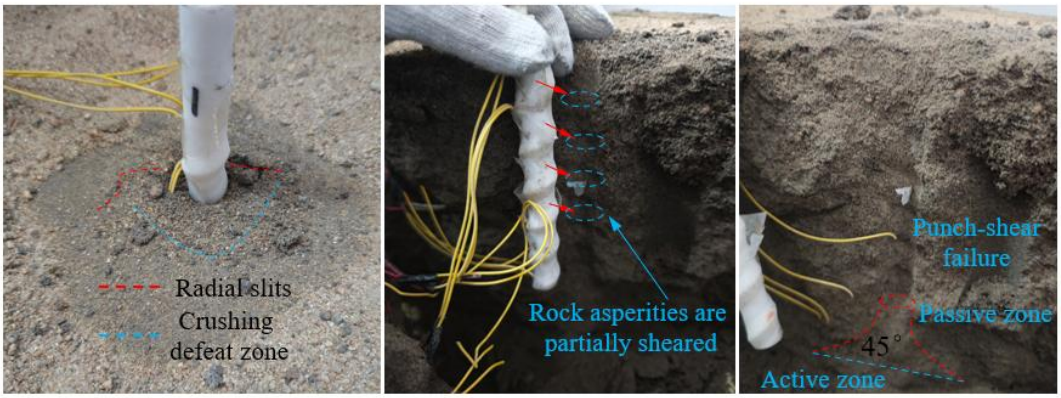
Five parallel experiments were conducted under identical conditions to ensure the repeatability of the results. Comprehensive data acquisition was performed throughout the testing process.

3 Test results and analysis

3.1 Failure mode

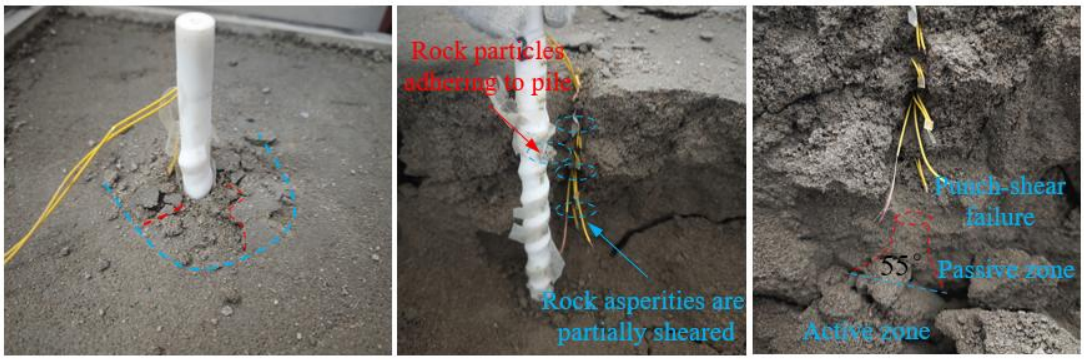
The failure mechanism of DRSPs under vertical load varies with position along the pile.

Examining the failure state of the model piles and the surrounding rock provides a clear understanding of the bearing mechanism. The failure modes observed at the rock top surface, the pile-rock interface (PRI), and the pile end for all five tests are presented in Fig. 10 (a) to (e).



Bedrock surface　　Pile-rock interface　　Pile bottom

(a) Pile No. 1



Bedrock surface　　Pile-rock interface　　Pile bottom

（b）Pile No. 2



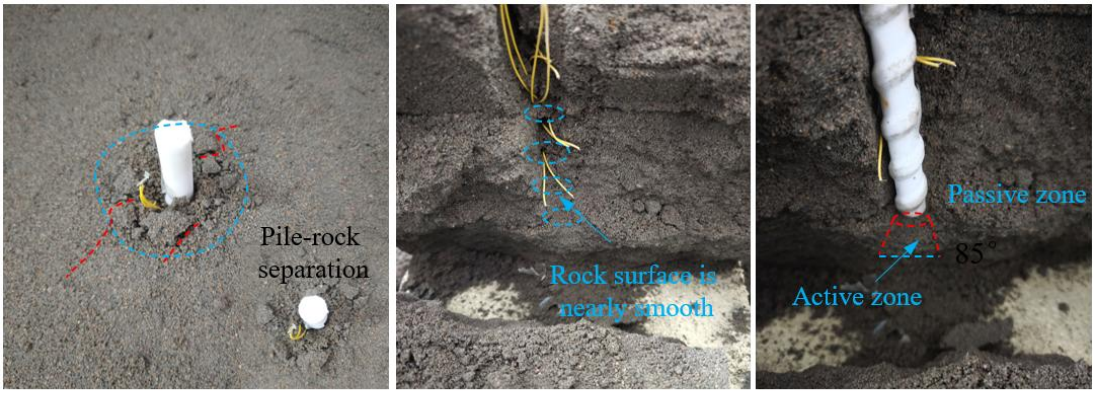
Bedrock surface　　Pile-rock interface　　Pile bottom

（c）Pile No. 3



Bedrock surface　　Pile-rock interface　　Pile bottom

（d）Pile No. 4



Bedrock surface　　Pile-rock interface　　Pile bottom

（e）Pile No. 5

Fig. 10 Failure modes of pile top, PRI and pile bottom

It can be seen from Fig. 10 that DRSPs with different roughness include the same failure mechanism when they fail: (1) A crushing zone appears on the bedrock surface accompanied by cracks parallel to the pile diameter. For DRSPs, since the boundary conditions of the rock-socketed part and the non-rock-socketed part are very different, the non-rock-socketed part is considered as an independent end-bearing pile, so the top of the bedrock can be regarded as the bearing stratum of the non-rock-socketed part. In addition, due to the existence of roughness, the pile surface bulge makes the surface bedrock shear in the downward movement, and radial cracks appear on the surface, and the cracks appear in the range of 1D–2D around the pile. (2) Upon separation of the model pile from the rock, it was observed that the rock asperities had been partially sheared off, with their tips remaining at a reduced height. The relative slip at the PRI

generated a distinct failure surface along a well-defined slip line. The degree of damage was more pronounced in the shallow region and diminished with increasing depth. (3) The failure mechanism at the pile tip was characterised by punching shear. This resulted in a wedge-shaped failure zone in the underlying rock, where the active wedge was oriented at approximately 45° to the pile axis. The extent of damage was highly non-uniform, severe rock crushing was evident in the passive zone, contrasting with the relatively intact rock mass in the active wedge.

With increasing roughness, the area of the crushed zone on the bedrock surface showed no significant variation across the five piles. The number and length of cracks on the surface of Piles No. 1 to No. 3 exhibited little change, generally confined within a 1D radius from the pile. In contrast, Piles No. 4 and No. 5 exhibited a greater number of cracks, which extended to a distance of 2D from the pile. Furthermore, as shown in Fig. 10 (c)-(e), an increase in the RF resulted in a larger volume of sheared rock asperities at the PRI and a downward shift of the failure plane. Regarding the pile tip, a higher RF correlated with a reduced failure zone. The depth of the shear failure decreased from 6D for Pile No. 1 to 2D for Pile No. 5, while the base angle of the triangular wedge failure zone increased from 45° to 90°.

3.2 Load-settlement curve

Table. 4 shows the displacement data of the top of five piles collected by dial indicator under various loads during the experiment. Fig. 11 shows the load-settlement curve of five piles drawn according to the data in the table.

Table. 4 Settlement of five piles under vertical load

Load level	Load (N)	Settlement (mm)				
		Pile 1	Pile 2	Pile 3	Pile 4	Pile 5
Load plate	110	0.15	0.05	0.05	0.05	0.03
1	310	0.275	0.15	0.1	0.1	0.07
2	510	0.43	0.29	0.26	0.25	0.14
3	710	0.63	0.35	0.33	0.3	0.24
4	910	0.75	0.48	0.42	0.38	0.32
5	1110	0.95	0.55	0.53	0.44	0.41

6	1310	1.35	1.02	0.62	0.53	0.49
8	1510			0.81	0.65	0.58
9	1710			1.23	0.75	0.7
10	1910				0.88	0.8
11	2110				1.2	0.9
12	2310					1.2

375

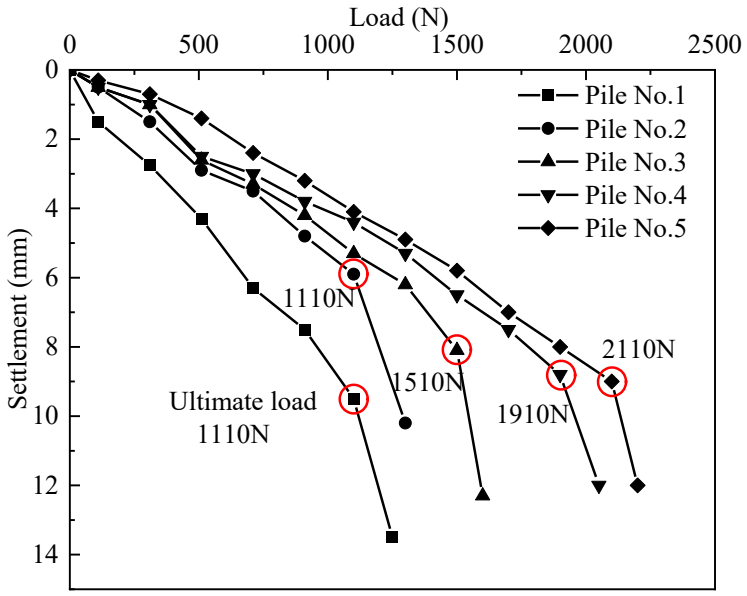


Fig. 11 Load-settlement curves of model piles under different roughness

376 As illustrated in Fig. 11, the ultimate bearing capacity of the model piles exhibits a
377 positive correlation with the shaft roughness coefficient. The load-settlement curves
378 can be delineated into two distinct stages: (1) Linear settlement stage. The settlement
379 of pile top is approximately linear with load, (2) Accelerated settlement stage. When
380 the load attains a specific threshold, the slope of the load-displacement curve steepens,
381 and a further load increment leads to a precipitous increase in settlement. The transition
382 point between these two stages defines the ultimate bearing capacity of the pile, as
383 indicated by the red zone in the Fig. 11. Piles No. 1 and No. 2 exhibited an identical
384 ultimate bearing capacity of 1110 N. Compared to Pile No. 1, the ultimate capacities of
385 Piles No. 3, No. 4, and No. 5 were higher by 26.7%, 42.1%, and 47.6%, respectively.
386 Furthermore, despite having nearly identical roughness coefficients (RF), Piles No. 2
387 and No. 3 showed a notable difference in bearing capacity of 400 N. The load-
388 settlement curves of Piles No. 3 to No. 5 demonstrated a similar developmental pattern.

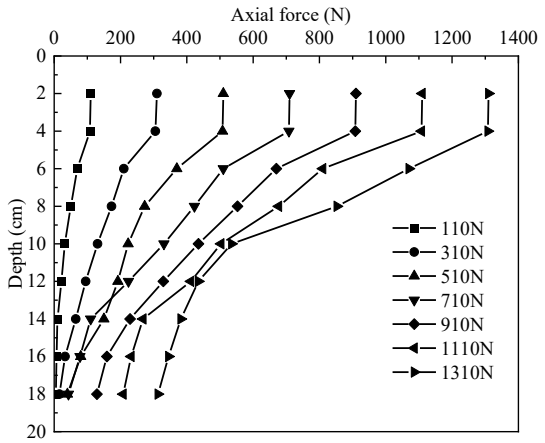
The PRI failure modes provide a clear mechanistic explanation for the load-settlement behaviour. Higher RF values led to more complete shearing of rock asperities, creating a smoother failure surface and accounting for the consistent settlement trend in Piles No. 3–5 before failure. A clear correlation was established: pile settlement decreased inversely with RF, evidenced by reductions of 32.6% to 67.4% compared to the smoothest pile (No. 1) at loads under 1110 N. Quantitatively, a 0.1 increment in RF resulted in an average 33.5% reduction in settlement and a 20% increase in ultimate capacity.

3.3 Axial force

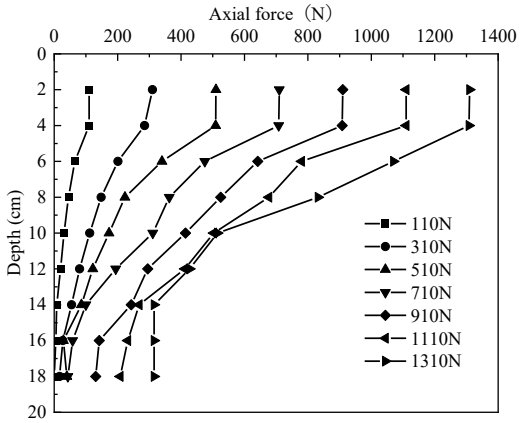
According to the deformation ΔL at the pile depth collected by the pile strain gauge, the pile axial force N can be calculated according to Eq. (9):

$$N = \Delta L \cdot E \tag{9}$$

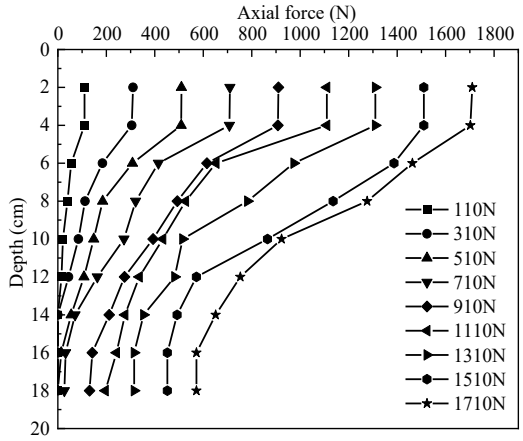
where E is Young's modulus of pile. Fig. 12 shows axial force curves of five piles.



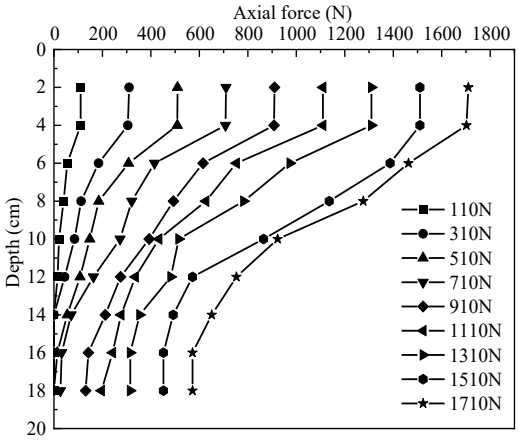
(a) Pile No.1



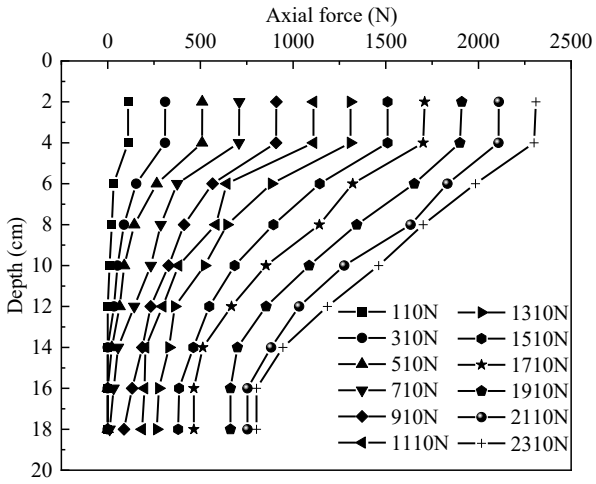
(b) Pile No.2



(c) Pile No.3



(d) Pile No.4



(e) Pile No.5

Fig. 12 Shaft force curves e under different roughness

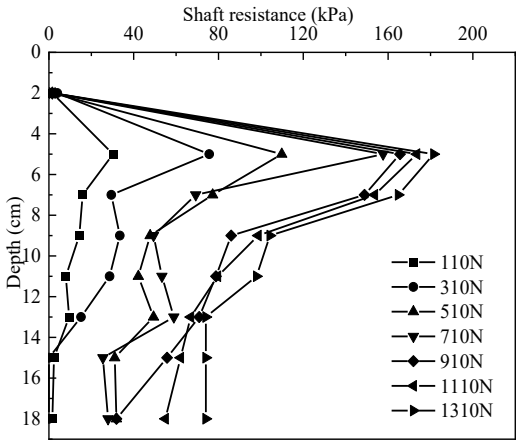
It can be observed from Fig. 12, the axial force remains constant within the top 0-5 cm of the pile, equalling the applied load at the head. Upon entering the rock stratum, the axial force begins to attenuate with depth. The rate of this attenuation increases with the RF, indicating that the shaft resistance plays an increasingly significant role in load transfer. For piles with a low RF, the axial force decreases gradually, suggesting that a large proportion of the load is carried by base resistance. This implies insufficient mobilisation of side resistance at the PRI, with load being transmitted primarily through the pile tip. In contrast, for piles with a high RF, the axial force decreases rapidly in the upper and middle sections, resulting in a relatively small end-bearing force. This demonstrates that a higher RF effectively enhances the frictional capacity of the PRI, leading to a more uniform distribution of load along the pile shaft.

3.4 Shaft resistance

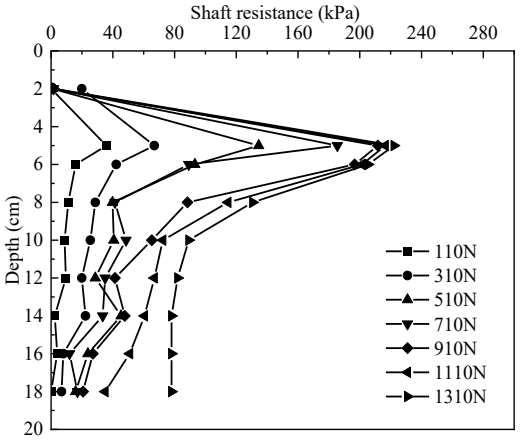
Based on the axial force of pile, the shaft resistance of single pile was calculated according to Eq. (10):

$$f_{\mathrm{i}} = \frac{N_{\mathrm{i}} - N_{\mathrm{i+1}}}{\pi D h} \tag{10}$$

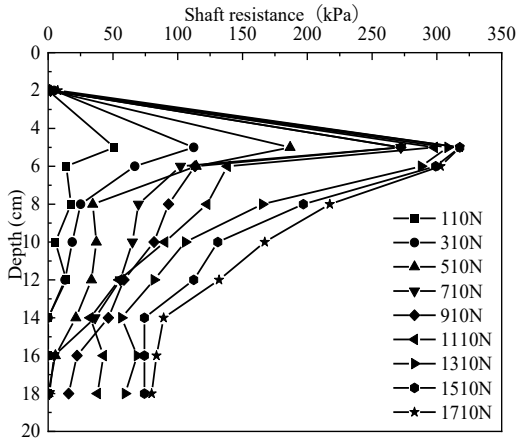
where N_{i} and $N_{\mathrm{i+1}}$ are axial forces at depth of i and i+1, respectively; D is the pile diameter; h is pile length from i to i+1; and f_{i} is the axis force at depth of i. Fig. 13 shows the distribution trend of side friction resistance per unit pile body calculated by Eq. (10) with depth.



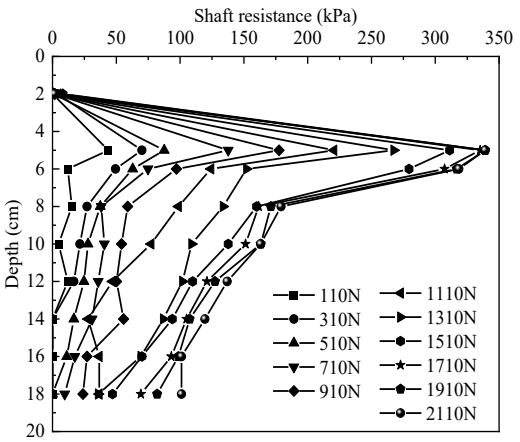
(a) Pile No.1



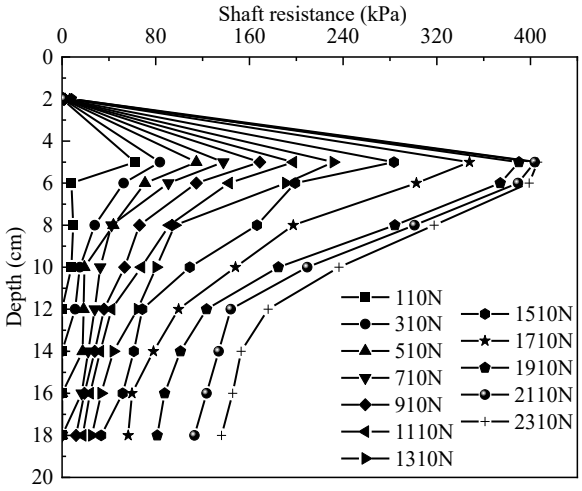
(b) Pile No.2



(c) Pile No.3



(d) Pile No.4



(e) Pile No.5

Fig. 13 The friction resistance curves of pile under different roughness

As shown in Fig. 13, the side friction resistance of the model piles with different roughness values exhibits a consistent trend with depth: it is zero in the top 0-5 cm

segment, increases abruptly upon entering the rock stratum, and then decreases progressively with further depth. Under low load, the side friction within the lower rock block segment (12–20 cm) for piles No. 1–5 is negligible, indicating that the resistance in this region has not yet been mobilised. As the load increases, the lower part of the rock socket begins to participate in carrying the external load. Concurrently, the relative displacement at the PRI in the upper rock block segment (5–7 cm) reaches a critical value, causing the side friction resistance in that zone to stabilise and not increase further.

For low-RF piles (No. 1–2), the PRI within the 5–7 cm depth range reached its ultimate friction resistance at a load of 1110 N. Although the ultimate resistance provided by pile No. 2 was 18.2% higher than that of pile No. 1, the depth range over which this maximum resistance was mobilised was greater for pile No. 1. This difference is attributed to the lower RF of pile No. 1, which resulted in a more gradual mobilisation of side friction along the socket length under the same load. Furthermore, the data confirm that the ultimate side friction increases with RF, with values of 320, 340, and 410 kPa for piles No. 3–5. Notably, despite a minimal difference in RF between piles No. 2 and 3, the ultimate side friction of pile No. 3 was 41.2% higher, an enhancement attributable to the specific morphology of the rock asperities. This influence is further supported by the 47.1% increase in ultimate friction for pile No. 4 compared to pile No. 2, underscoring the significant effect of asperity geometry on the shear characteristics of the PRI.

4 Bearing capacity of DRSPs

4.1 Relationship between bearing capacity of DRSPs and RF

It is widely recognised that the ultimate capacity of DRSPs derives from both end-bearing and shaft friction at the PRI, the distribution of which is primarily controlled by the RF. Notwithstanding this, prevailing design codes persist in modelling the PRI as a smooth interface, effectively ignoring the critical role of RF. This constitutes a significant oversimplification that results in unduly conservative and potentially uneconomical designs due to the under-verification of capacity.

The model test results demonstrate a significant positive correlation between the ultimate bearing capacity Q_u of DRSPs and the interface RF. Furthermore, increases in the rock-socketed depth h_r and the rock's compressive strength σ_c also enhance the bearing capacity. To quantify the relationship for Q_u, a dimensionless analysis was

454 performed by incorporating the pile diameter D and the elastic modulus of the pile E_p
455 in accordance with the π principle, leading to the following relationship

$$\pi_1 = \frac{Q_u}{\sigma_c D^2}, \pi_2 = \mathrm{RF}, \pi_3 = \frac{h_r}{D}, \pi_4 = \frac{E_p}{\sigma_c}$$
$$\frac{Q_u}{\sigma_c D^2} = f\left(\mathrm{RF}, \frac{h_r}{D}, \frac{E_p}{\sigma_c}\right) \tag{11}$$

456

457 Table. 5 Ultimate bearing capacity of model pile and prototype pile

RF	Ultimate bearing capacity Q_u	
	Experiment	Predicted
0.051	1110	1101.87
0.054	1110	1228.46
0.058	1510	1420.15
0.066	1910	1897.93
0.071	2110	2275.07

458 The ultimate bearing capacity Q_u of model pile and prototype pile embedded in rock
459 under different RF is shown in
460 Table. 5. Based on the data in
461 Table. 5, the relationship between the Q_u and RF of DRSPs is fitted:

$$Q_u = 0.36 \cdot \sigma_c D^2 \cdot e^{36.25 \cdot \mathrm{RF}} \tag{12}$$

462 Fig. 14 shows the comparison between the experimental and predicted bearing capacity
463 values for model piles No.1-5. It can be seen that Eq. (12) can effectively predict the
464 ultimate bearing capacity of DRSPs with an average absolute error of about 8.8%,
465 which is within the acceptable range.

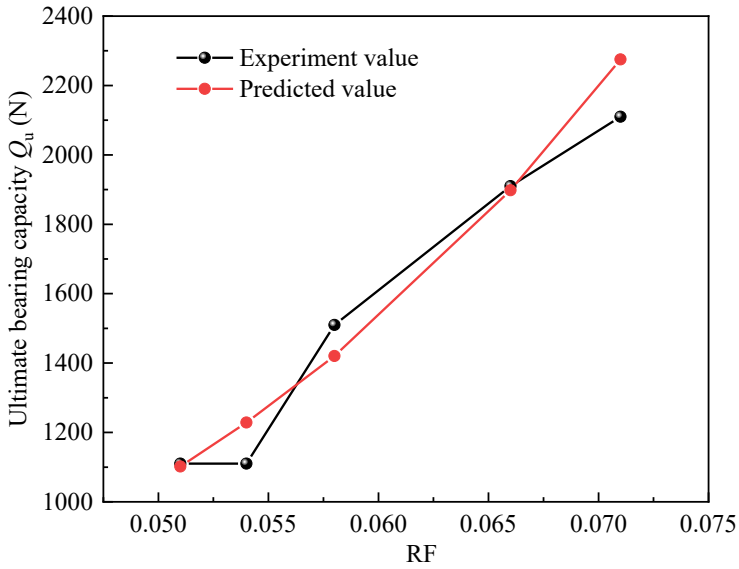
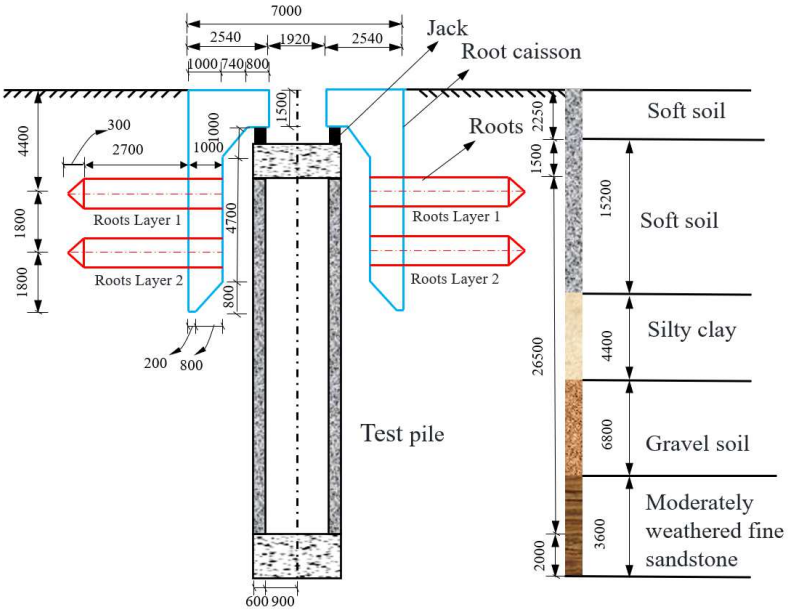


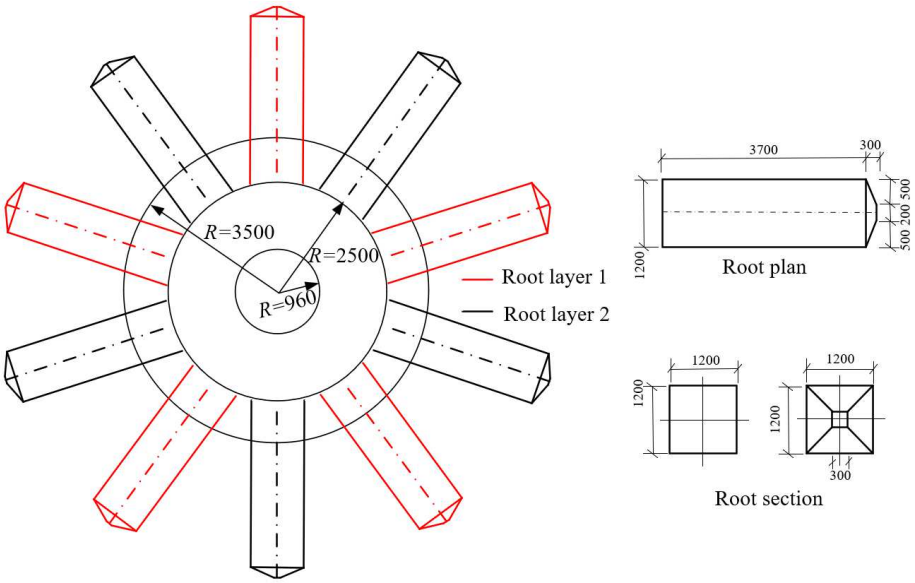
Fig. 14 Comparison between experimental and calculated values of model pile bearing capacity

4.2 Field test of RSPs

Qingshanhe Bridge is located in Maanshan City, Anhui Province, China. During the foundation construction of Qingshanhe Bridge, the vertical bearing capacity of YZK-8 large diameter hollow pile near pile position K59+11 of main tower was tested in situ. The pile outer diameter is 3.0m, the wall thickness is 60cm, and the pile length is 30.0m. The underground open caisson is used as bearing system to provide reaction force for test pile. The test pile and open caisson structure are shown in Fig. 15.



（a）Size of test pile and root caisson



（b）Root placement and size

Fig. 15 Detailed structure of test pile and root caisson

473

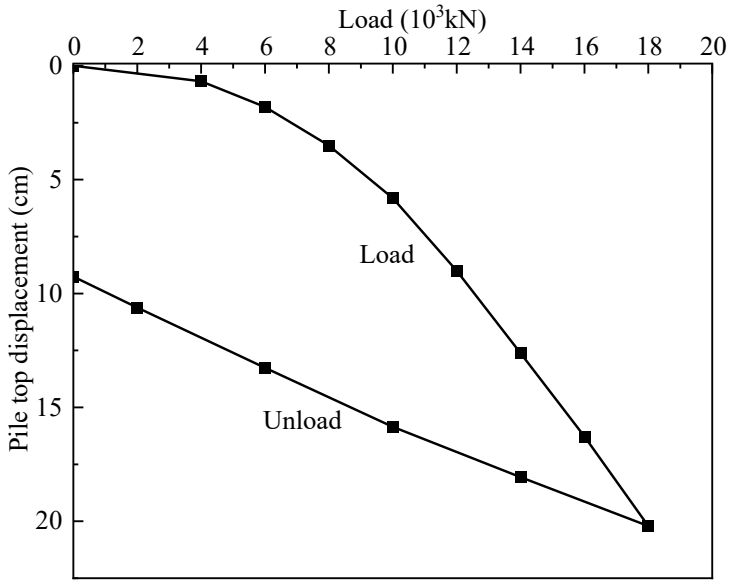


Fig. 16 load-settlement curve of test pile

The test pile was socketed 3.6 m into moderately weathered sandstone with a compressive strength of 4.66 MPa. The load-settlement curve for this pile is presented in Fig. 16, indicating an ultimate bearing capacity of approximately 18,000 kN. As direct in-situ measurement of the RF is challenging, the value for the test pile was estimated using Eq. (6). Given the similarity in hole formation methods between the test pile and the bridge piles, the rock joint characteristics shown in Fig. 1(a) were adopted as a proxy for the pile wall roughness. This yielded an RF value of 0.0021. The predicted ultimate bearing capacity of the test pile, based on this RF, is

$$\begin{aligned} Q_{\mathrm{u}} &= 0.36 \cdot \sigma_{\mathrm{c}} D^2 \cdot \mathrm{e}^{36.25 \cdot \mathrm{RF}} \\ &= 0.36 \times 4.66 \times 3^2 \times \mathrm{e}^{36.25 \times 0.0021} = 16293\mathrm{kN} \end{aligned} \tag{13}$$

A discrepancy of 9.49% was observed between the predicted and experimental bearing capacities. This discrepancy is likely attributable to two primary factors. Firstly, the contribution of the overlying soil layers to the overall bearing capacity was not accounted for in the prediction model. Secondly, with a rock-socketed ratio h_{r} of 1.2, the test pile does not fall within the classification of a DRSPs. Consequently, the load distribution mechanism differs significantly from that of a typical DRSP, which may also contribute to the observed variance.

5 Conclusions

This study employed similarity theory to investigate the bearing mechanism of DRSPs through indoor model tests. We designed five model piles with different RF, producing the piles via 3D printing and simulating the bedrock with a specific cement mortar mix.

By applying graded loads, we examined the failure modes and load-transfer mechanisms under varying RF conditions. The principal findings are summarised as follows:

(1) The failure of the DRSPs was characterised by the formation of crushing zones and radiating cracks on the rock surface. At the PRI, rock asperities were sheared off, with fragments remaining lodged in the pile's indentations. The pile tip failed in a punching shear mode, generating a triangular wedge-shaped failure zone in the underlying rock mass. Furthermore, increased roughness significantly influenced the failure mechanism: it led to more extensive surface cracking, a larger volume of sheared rock at the PRI, and a more localised failure at the pile tip. Specifically, the depth of the tip failure zone decreased, while the base angle of the failure wedge increased from 45° to 90°.

(2) The ultimate bearing capacity of the DRSPs exhibited a positive correlation with the RF, whereas the pile head settlement demonstrated a negative correlation. The model tests quantified this relationship, showing that an increment of 0.1 in the shaft RF resulted in an average increase of 20% in the bearing capacity and a corresponding average reduction of 18% in the settlement.

(3) Increased shaft roughness promoted a more efficient transfer of load to the surrounding rock via shaft resistance, as evidenced by a faster attenuation of axial force and a concurrently higher ultimate side friction at the PRI.

(4) A strong positive correlation between the RF and Q_u of DRSPs. A validated predictive model integrates RF, D, E_p, h_r, and σ_c, with 8.8% average error. Field tests showed a 9.49% deviation but confirmed the RF trend.

Statements and Declarations

Competing Interests

The authors declare that they have no conflicts of interest.

Data availability

All data generated or analyzed during this study are included in the article.

References

Ai ZY, Chen YF (2020) FEM-BEM coupling analysis of vertically loaded rock-

socketed pile in multilayered transversely isotropic saturated media. Computers and Geotechnics 120:103437
Akguner C, Kirkit M (2011) Comparison of Rock-Socketed Pile Capacities Obtained from Load Testing and Empirical Methods. Tek Dergi 22(4):5713-5723
Arnold P, Fenton GA, Hicks MA (2012) Modern geotechnical design codes of practice: implementation, application and development. IOS Press,
Chen RY, Yin YG, He M (2025) Modification of Bearing Capacity of Rock-Socketed Pile: Considering Concrete–Rock Interface Roughness and Initial Stress of Concrete. Transp Res Rec:355278511
Dai GL, Salgado R, ASCE F, Gong WM et al (2017) The effect of sidewall roughness on the shaft resistance of rock-socketed piles. Acta Geotech 12(2):429-440
Dykeman P, Valsangkar AJ (1996) Model studies of socketed caissons in soft rock. Can Geotech J 33(5):747-759
Goodier JN, Thomson WT (1944) Applicability of similarity principles to structural models. National Advisory Committee for Aeronautics,
Gutiérrez-Ch JG, Melentijevic S, Senent S, Jimenez R (2025) DEM modelling of shaft load transfer behavior of rock-socketed piles. Computers and Geotechnics 181:107149
Gutiérrez-Ch JG, Song G, Heron CM, Marshall A et al (2021) Centrifuge tests on rock-socketed piles: effect of socket roughness on shaft resistance. J Geotech Geoenviron Eng 147(11):4021125
Horvath RG, Kenney TC, Trow WA (1980) Results of tests to determine shaft resistance of rock-socketed drilled piers. In: International Conference on Structural Foundations on Rock, 1980, Sydney, Australia.,
Hou JC, Zhao H, Peng WZ, Zhao MH (2022) A limit solution for predicting side resistance on rock-socketed piles. J Eng Mech 148(1):4021131
Huang B, Zhang YT, Fu XD, Zhang BJ (2019) Study on Visualization and Failure Mode of Model Test of Rock-Socketed Pile in Soft Rock. Geotech Test J 42(6):1624-1639
Huang B, Zhang YT, Lv B, Yang ZJ et al (2021) Vertical bearing characteristics of rock-socketed pile in a synthetic soft rock. Eur J Environ Civ Eng 25(1):132-151
Johnston IW, Choi SK (1986) A synthetic soft rock for laboratory model studies. Geotechnique 36(2):251-263
Kulkarni RU, Dewaikar DM (2019) Analysis of rock-socketed piles loaded in axial compression in Mumbai region based on load transfer characteristics. Int J Geotech Eng 13(3):261-269
Li YF, Zhao JH, Xiong Y, Wang QH (2021) Experimental and theoretical research on large-diameter rock-socketed pile embedded depth. Arch Civ Eng 67(2)
Liang R, Yin ZY, Yin JH, Wu PC et al (2024) An enhanced micromechanical rock–pile interface model with application to rock-socketed pile modeling. Int J Numer Anal Methods Geomech 48(11):2971-2995
Liu J, Li ZW, Dai GL, Gong WM (2023) Field measurement and theoretical analysis of sidewall roughness on shaft resistance of rock-socketed piles. J Mar Sci Eng 11(8):1622

Liu L, Xiao L, Liu Y, Zhao MR et al (2025) Horizontal Bearing Characteristics of Large-Diameter Rock-Socketed Rigid Pile and Flexible Pile. BUILDINGS-BASEL 15(5)

Murali AK, Haque A, Bui HH (2024) Advancing Rock-Socketed Pile Design with a Unified Interface Shear Strength Framework for Soft Rocks. Rock Mech Rock Eng 57(9):7253-7269

Rui G, Yan QW, Jun Y (2011) Model test of socketed depth's influence on bearing mechanism in rock-socketed pile. Applied Mechanics and Materials 90-93:332-336

Seol H, Jeong S, Kim YM (2009) Load transfer analysis of rock-socketed drilled shafts by coupled soil resistance. Computers and Geotechnics 36(3):446-453

Singh AP, Bhandari T, Ayothiraman R, Rao KS (2017) Numerical analysis of rock-socketed piles under combined vertical-lateral loading. Procedia engineering 191:776-784

Sivaraman S, Kumaran M (2023) Challenges in the Construction of Deep Rock Socketed Pile for Urban Infrastructure. In: DFI-India Annual Conference. Springer, pp 343-351.

Sun ZJ, Han YF, Liu F, Min R (2024) Sensitivity Analysis of Influencing Factors of Vertical Bearing Capacity of Rock-Socketed Piles Based on Orthogonal Test. In: Frontier Research on High Performance Concrete and Mechanical Properties. Springer, pp 93-106

Sun ZJ, Liu F, Han YF, Min R (2024) Prediction of ultimate bearing capacity of rock-socketed piles based on GWO-SVR algorithm. Structures 61

Takahashi H, Ikeno M (2024) Concept of the Law of Similarity in Model Tests. In: Theory and Application of Hydraulic Modeling. CRC Press, pp 72-109

Wan ZH, Duan C, Hu T, Zhou F et al (2024) Field Study on Bearing Capacity of Large-Diameter Rock-Socketed Bored Piles with Combined Grouting in Highly Weathered Rock Layers. Rock Mech Rock Eng 57(10):8701-8722

Wang KY, Shen B, Zhao XL (2023) Journal of Highway and Transportation research and Development. Journal of Highway and Transportation research and Development 40(05):106-115

Wang QY, Xiong ZB, Zhang JS, Chen XB (2011) Model tests on resistance behaviors of rock-concrete interface of rock-sockted piles in red-sandstone rock. Chinese Journal of Geotechnical Engineering 33(04):661-666

Xing HF, Han J, Li CF (2017) Performance monitoring of super large-diameter rock-socketed piles by optic fiber sensors. Mater Test 59(6):585-590

Xing HF, Xiong F, Wang LJ, Luo Y (2017) Research on shaft resistance of rock-socketed piles based on the cavity expansion theory. Mar Geores Geotechnol 35(6):873-877

Xing HF, Zhang Z, Meng MH, Luo Y et al (2014) Centrifuge Tests of Superlarge-Diameter Rock-Socketed Piles and Their Bearing Characteristics. J Bridge Eng 19(6)

Xu F, Dai GL, Gong WM, Zhao XL et al (2022) Lateral Loading of a Rock-Socketed Pile Using the Strain Wedge Model Based on Hoek-Brown Criterion. Appl Sci

(Basel) 12(7)
Xu XS, Zhong WX, Zhang HW (1997) The Saint-Venant problem and principle in elasticity. Int J Solids Struct 34(22):2815-2827
Yalin MS (1971) Principles of the theory of similarity. In: Theory of Hydraulic Models. Springer, pp 35-50
Yan N, Hao ZM, Bai XY, Cui L et al (2025) Load-bearing characteristics and optimization design for rock-socketed bored piles in sandy silty clay in coastal areas. Soil Dyn Earthq Eng 190
Zhang H, Tannant D, Xing HF, Zhu L et al (2025) Centrifuge model tests on the bearing behavior of large-diameter rock-socketed pile group in valley area. Bull Eng Geol Environ 84(6):331
Zhang RL, Xue XH (2024) A novel hybrid model for predicting the end-bearing capacity of rock-socketed piles. Rock Mech Rock Eng 57(11):10099-10114
Zhao H, Xiao Y, Zhao MH, Yin PB (2017) On behavior of load transfer for drilled shafts embedded in weak rocks. Computers and Geotechnics 85:177-185
Zhao MH, Xia RY, Yin PB, Yang CW et al (2014) Load transfer mechanism of socketed piles considering shear dilation effects ofsoft rock. Chinese Journal of Geotechnical Engineering 36(06):1005-1011
Zhao XL, Melentijevic S, Shen YP, Sun ZK et al (2024) Experimental study of the effects of the void located at the pile tip on the load capacity of rock-socketed piles. Sci Rep 14(1)
Zhao XL, Shen YP, Melentijevic S, Sun ZK et al (2024) The Load-Bearing Mechanism of Rock-Socketed Piles Considering Rock Fragmentation. Rock Mech Rock Eng 57(11):10071-10097